Surface Microscopy of Atomic and Molecular Hydrogen from Field-Evaporating Semiconductors

Lorenzo Rigutti, Enrico Di Russo, Florian Chabanais, Ivan Blum, Jonathan Houard, Noëlle Gogneau, Ludovic Largeau, Alexander Karg, Martin Eickhoff, Williams Lefebvre, et al.

Surface Microscopy of Atomic and Molecular Hydrogen from Field-evaporating Semiconductors

Lorenzo Rigutti[1*], *Enrico Di Russo*[1], *Florian Chabanais*[1], *Ivan Blum*[1], *Jonathan Houard*[1], *Noëlle Gogneau*[2], *Ludovic Largeau*[2], *Alexander Karg*[3], *Martin Eickhoff*[3], *Williams Lefebvre*[1], *François Vurpillot*[1].

[1] UNIROUEN, CNRS, Groupe de Physique des Matériaux, Normandie Université, 76000 Rouen, France.

[2] Centre de Nanosciences et de Nanotechnologies, CNRS UMR 9001, Univ. Paris-Sud, Université Paris-Saclay, C2N – Orsay, 91405 Orsay Cedex, France.

[3] Institute of Solid State Physics, University of Bremen, 28359 Bremen, Germany.

* Corresponding author: lorenzo.rigutti@univ-rouen.fr

KEYWORDS: Hydrogen, Atom Probe Tomography, Surface Chemistry, Field ionization, Field Emission

ABSTRACT

We report on the microscopic behavior of residual hydrogen on nanometric field emitters. By using homogeneous or heterostructured semiconductor specimens analyzed in laser-assisted atom probe, it is possible to study how the relative abundances of the ionic species H^+, H_2^+, H_3^+ depend on the microscopic electric field, estimated through post-ionization statistics. In the case of Ga-containing semiconductors, the relative abundances of H^+, H_2^+ and H_3^+ follow a common trend, independently of the non-metallic component of the matrix. The dependence of the total H flux on the electric field exhibits a more complex behavior, which depends also on the spatial

direction of the variation of the field (in-depth or on-surface). The analysis of multiple detection events provides further insight into surface chemistry. Noticeably, H^+-H_3^+ ion pairs are both correlated in number and separated by very small distances on the detector space, suggesting a possible reaction $2H_2 \rightarrow H_3^+ + H^+ + 2e^-$ taking place on the field emitter surface.

1. Introduction

Increasing attention is paid to hydrogen due to its importance as an energy vector [1]. Beyond that, it plays an important role in the determination of structural properties in metals [2–4] and interacts with functional defects in semiconductor bulk and surfaces [5,6].

The potential of Atom Probe Tomography (APT) for an in-depth study of hydrogen is related to its capability of analyzing chemical species evaporating from the surface of a field emitter specimen, allowing for their localization in 3D and their chemical identification. However, there is a major issue concerning hydrogen because it is usually found in its gaseous H_2 form within the analysis chamber. This gas becomes polarized close to the field emitter, may dissociate on the emitter surface and be ionized either by the static electric field applied to the surface or during the laser or voltage pulse which trigger the ion evaporation from the matrix. In the first case, hydrogen contributes to the background noise in the mass spectrum, which degrades the chemical sensitivity of the analysis. In the second case, H-related ionic species (H^+, H_2^+ and H_3^+) contribute to the formation of well-identifiable signals on the mass spectrum. This signal perfectly overlaps with the possible signal of H contained within the material under study, hindering its identification, localization and quantification. This is the reason why different strategies are being developed in order to tackle the problem of parasitic hydrogen in atom

probes. Among the possible approaches, one can remind the elimination of parasitic hydrogen, for instance by accurate choice of the materials and coating of the analysis chamber [7], or by deuterium charging of specimens[3,4,8]. The issues related to parasitic hydrogen in atom probe may also concern its interaction with surface atoms from the materials, as it is known to modify the evaporation field [9] and to react with the surface by forming hydride molecular ions [10]. Understanding the behavior of parasitic hydrogen is motivated by three main aspects. First, it may be useful in statistically discriminating the behavior of parasitic hydrogen from that of hydrogen contained within the material[11]. The second is that the behavior of residual hydrogen under high electric field may have a perspective interest in surface chemistry and molecular physics, including the time-controlled production of selected hydrogenic ion species (for instance, H_3^+ is an ionic species of interest for astronomy, as it is found in the interstellar space [12,13]) and hydrides. As a third point, the ratio of atomic and molecular hydrogen may represent a robust and universal indicator of the surface electric field on any atom probe specimen. As this parameter is crucial for the reliability of APT analyses and for their compositional metrology, with a particular interest for emerging applications based on frozen water samples[14,15]. Beyond the importance of hydrogen quantification in classical systems, i.e. functional semiconductors or structural materials, further interest could arise for the analysis of hydrogen in emerging materials, for instance metal hydrides, or polymers (including organic semiconductors).

In fact, APT is based on the evaporation of atoms from a surface exposed to a high electric field, of the order of 20-40 V/nm. In laser-assisted APT, the laser promotes the evaporation through the injection of a thermal pulse which does not significantly modify this field[16]. These atoms, even when not evaporating, may react with field-adsorbed atoms or catalyze reactions between adsorbed atoms from the gas phase. Field ionization of such gases, on the other hand, is at the

basis of field ion microscopy (FIM). Due to these features, field desorption-related techniques have been extensively applied in the past for the study of gas reactivity on surfaces [17,18]. More recently, APT has been considered as a tool for the study of surface and sub-surface reactions. Field-emission tip samples may indeed be exposed to reactants in purposely designed cells (which can also be used for charging the samples with highly diffusive species such as H) [19] before being directly transferred to the APT analysis chamber. This technique known as the in-situ atom probe, allows for the in-depth profiling of phases obtained by chemical reactions[20] or for the study of the interaction between highly diffusive species and structural defects or impurities[21]. Beyond the "in-situ" APT, the so-called "operando" APT may be applied (both these terms, "in-situ" and "operando" are to be interpreted in a "chemical" sense – other "in-situ" and "operando" meanings for APT-related techniques exist, see for instance the recently demonstrated Photonic Atom Probe[22,23]), which is an update of pulsed field desorption mass spectrometry[24], in which chemical reactions are studied in a dynamical way, i.e. collecting surface reaction products as a function of environmental parameters, such as voltage or laser pulse repetition frequency.

As a complement to these approaches, we notice that progress in hardware and data mining methods makes it currently possible to study gas-surface interactions and reactions even in the case when parasitic H has a reduced impact on standard APT measurements. For instance, it becomes possible (*i*) to analyze 3D APT data, monitoring the variations of the electric field across different phases within the same specimen and to compare them to the fractions of atomic and molecular hydrogen detected; (*ii*) to analyze the presence of H-related species within multiple detection events and correlations between them through the whole mass spectrum. This allows getting insight on the chemical reactions that may take place on the surface. Furthermore,

the development of methods based on multiple hit detection could be extended to the "operando" APT, allowing for an extension of the time resolution of the technique, which would no longer be limited by the pulse repetition frequency but rather by the temporal resolution of the detector. This may have a perspective application in the study of heterogeneous field-assisted catalysis[25].

This contribution studies microscopic phenomena relative to residual parasitic hydrogen detected in the mass spectra of evaporating field emitters. We address three main aspects relative to the detection of residual hydrogen in APT analyses. We focus indeed *(i)* on the relative abundance of the different hydrogenic ion species, *(ii)* on the dependence of its amount on the surface electric field, and on *(iii)* selected aspects of the surface chemistry of H_2. Our method is based on the analysis of homogenous or heterostructured semiconductors containing the metallic Ga element, which allows for the estimation of the surface electric field in a wide interval through the so-called charge state statistics for Ga [26,27]. The surface chemistry of hydrogen is investigated through the analysis of multiple detection events, which account for H_2-related chemical reactions.

2. Methods

2.1. Analyzed systems

The common feature of the materials systems analyzed in this work is that all are compound semiconductors containing gallium (Ga), fabricated or grown as planar films. The materials have been chosen in such a way that their cohesive energy and their evaporation field span quite a large interval. This translates into APT analyses in which the surface field varies approximately

between 22 and 27 V/nm, starting from GaAs (low field) up to Ga_2O_3 (high field). The samples have different origin and growth processes.

2.1.1. GaAs

The GaAs sample was a nominally undoped, (100)-oriented substrate purchased from Freiberger Compound Materials.

2.1.2. (Al,Ga)N

The (Al,Ga)N samples were grown by molecular beam epitaxy (MBE) at former LPN Marcoussis (now C2N Saclay), all samples are grown along the polar c-axis. These samples contain superlattices with 20 periods of 20 nm layers of $Al_yGa_{1-y}N$/GaN, with either y = 0.07 or y = 0.16. This alternation of layers has been purposely designed for APT metrology experiments, in order to monitor the variation of measured composition in specimens containing higher and lower field layers. Further details and results issued from these structures are reported in ref. [28].

2.1.3. Ga_2O_3

The Ga_2O_3 samples were extracted from thin films grown by plasma-assisted MBE on (001)-oriented sapphire substrates in a Riber Compact 12 system at the growth temperature of 700 °C. Further details about the growth and the features of these systems may be found in ref. [29].

2.2. Laser-assisted Atom Probe Analysis

Atom Probe tip specimens were obtained by standard lift-off and annular milling procedures based on focused ion beam (FIB)[30]. All analyses were conducted in a laser-assisted wide-angle

tomographic atom probe (LaWATAP). The light used for the control of the evaporation in time was either IR light at 1030 nm (in the case of GaAs) or UV light at 340 nm from a pulsed laser (pulse duration 350 fs) focused on ~60 µm diameter spot at a laser repetition frequency f_{laser} = 100 kHz. During measurements the laser pulse energy E_{las} ranged between 5 and 60 nJ, (the pulse energy E_{las} = 1 nJ corresponds roughly to an average pulse intensity I_{las} = 0.22 W µm^{-2}). The detection system was a multi-channel plate/advanced delay line detector (MCP/aDLD) with a MCP efficiency $\eta_{MCP} \approx 0.6$ [31,32]. It should be underlined that the multiple-hit detection capabilities of the aDLD system is crucial in this study, as all conclusions about the surface chemistry are possible only when a statistically significant number of multiple correlated detection events (i.e., events detected following the same laser pulse) is available.

Throughout the different analyses, the pressure in the chamber was in the range $5 \cdot 10^{-11}$ – $5 \cdot 10^{-10}$ mbar. These are the typical ultra-high vacuum conditions compatible with APT operation. We can assume that such pressure was mostly related to the presence of parasitic H_2.

2.2.1. Experimental conditions

The experimental details about the analyses of the different systems are reported in table 1. Two types of measurements have been performed:

A) Extensive analyses at constant detection rate. The total number of ions collected is of the order of several tens of millions. In this type of analysis, there are two counteracting phenomena, both related to the increase of the sample apex curvature radius during the analysis – a consequence of the non-zero shank angle of the tip: on one hand, the imaged surface area increases, and the net evaporation flux with it; on the other hand, the electric field decreases due to the increase of the apex radius. The DC voltage V_{DC} changes thus

in order to balance these two effects: it increases during the analyses, but its increase corresponds to a net decrease of the electric field. In dielectrics, such analyses may imply a decrease in the surface field up to 10 - 20 %[28].

B) Parametric analyses performed varying the laser energy and the applied DC voltage in order to keep the detection rate constant. These analyses are typically performed in order to monitor possible variation in the composition measurements in APT analyses[27,33].

All measurements were conducted at constant temperature, either 50 K or 80 K. The role of the temperature on the microscopic behavior of hydrogen was not studied, but it should be kept in mind that this parameter may also influence gas ionization rates, reaction rates involving hydrogen species only or hydrogen and atoms from the sample matrix, and evaporation rates. Volume reconstructions have been performed by taking into account the effective shape of the tip specimen and the actual layer thicknesses, assessed through preliminary TEM analysis as reported in ref. [28]. They provide a microscopic reference frame in which it is possible to highlight the variation of the relevant quantities introduced in the next section.

2.2.2. Relevant quantities

The relevant quantities for this study can be all defined over microscopic regions of the detector space (user- and software-defined pixels) or of the reconstructed space (user- and software-defined volume elements, or *voxels*), and can thus be exploited in order to study the microscopic behavior of the hydrogen molecular ions. The quantities are the following:

- The relative abundances of hydrogen molecular ions, defined as

$$A(\mathrm{H}_i^+) = \frac{n(\mathrm{H}_i^+)}{n(\mathrm{H}^+)+n(\mathrm{H}_2^+)+n(\mathrm{H}_3^+)}, \qquad (1)$$

Where i = 1,2,3 is the number of protons in the species (in the present notation $H_1^+ = H^+$) and n(X) represents the total number of species identified as X (which can be a specific ion or an elemental or molecular species) counted in the defined interval of detector or reconstructed space.

- The cumulative abundance of hydrogen species with respect to the number N of detected ions from all species:

$$\Phi(\mathrm{H}) = \frac{\left(n(\mathrm{H}^+)+n(\mathrm{H}_2^+)+n(\mathrm{H}_3^+)\right)}{N} \qquad (2)$$

- The Al III-site fraction, used for the characterization of the (Al,Ga)N samples containing superlattice structures.

$$y = \frac{n(\mathrm{Al})}{(n(\mathrm{Al})+n(\mathrm{Ga}))} \qquad (3)$$

- The Ga charge state ratio,

$$CSR(\mathrm{Ga}) = \frac{n(\mathrm{Ga}^{++})}{n(\mathrm{Ga}^{+})} \qquad (4)$$

which is used as a parameter allowing the estimation of the surface electric field according to the theory of post-ionization statistics [26]. The use of this parameter as a field indicator has been adopted in a large number of recent studies [27,34,35,33,28,36], in which its advantages and limitations were thoroughly discussed (e.g. see section 3 of ref. [28]). In the present study, the main advantage of the *CSR*(Ga) is that it may be exploited as a microscopic field indicator.

Table 1. Experimental conditions for the analyzed materials systems

System	Sample	Description	Type of Measu-rement	Base Temperature during APT analysis (K)	Detected Ions $x10^{-6}$	Effective Field Range (V/nm)	Fraction of H ions (%)
GaAs	1	Epitaxial layer	A	50	44	22-22.5	3.2
	2	Epitaxial layer	B	50	16	22-22.5	1.5
(Al,Ga)N	1	$GaN/Al_{0.07}Ga_{0.93}N$ superlattice	A	80	13	20.5-24	7.2
	2	$GaN/Al_{0.16}Ga_{0.84}N$ superlattice	A	50	32	23-25	3.3
	3	$GaN/Al_{0.16}Ga_{0.84}N$ superlattice	A	50	17	24-26	2.1
Ga_2O_3	1	Epitaxial layer	A	80	0.8	~27	1.5
	2	Epitaxial layer	B	80	1.1	~27	1.6

Legend. Type of measurement. A: Extensive acquisition at constant detection rate with field variation induced by the evolution of specimen geometry; B: Series of acquisitions at constant detection rate with field variation set by the user through the variation of the intensity of the triggering laser.

2.2.3. Mass spectra

The typical mass spectra of GaAs, (Al,Ga)N, and Ga_2O_3 are shown in in fig. 1. The spectral region corresponding to the three hydrogen molecules has been expanded in order to highlight

their heights and their different abundances in the three materials systems. It can be noticed that there is a majority of H_2^+ ion in GaAs, then the majority species becomes H^+ in the higher-field materials. H_3^+ is present in all spectra at systematically lower abundance. However, it appears to be more present at lower field in GaAs. The part of the mass spectra originating from the matrix of the material presents standard features.

In the case of GaAs (fig. 1-(a)), the two peaks associated to Ga^+ (resp. Ga^{2+}) isotopes are observed at 69 and 71 (resp. 35 and 35.5) Da. A peak associated to As appears at 75 (resp. 37.5) Da for the 1+ (resp. 2+) ionization state. Finally, 113 was assigned to As_3^{2+} molecular ions. Further As-containing ion clusters can be found at higher mass/charge values. Finally, it should be noticed that using low E_{las} and high V_{DC} the spectrum is affected by a significant background noise, which is related to DC field evaporation (i.e., between laser pulses).

In the case of the (Al,Ga)N-1 sample show in fig. 1-(b), the main constituent species found are Al^{1+}, Al^{2+}, Al^{3+}, Ga^{2+}, Ga^{1+}, N_2^+ and N_2^{2+}. Molecular species, such as AlN_2^+, and GaN_3^{2+} also contribute to the determination of the composition of the sample. Parasitic species other than hydrogen, such as carbon- and water-related peaks are also present, most likely supplied by the environment, by the Pt-C soldering deposited during the preparation of the tip by FIB or by some other unidentified sources.

In Ga_2O_3 (fig. 1-(c)), the two peaks associated with Ga^+ isotopes are observed at 69 and 71 Da (35 and 35.5 Da for Ga^{2+}), and the highest number of events is represented by doubly charged ions. Gallium could also be evaporated in weak proportions as Ga^{3+} ions (peak at 23 and 23.33 Da). The peak at 16 Da is due to O^+ and peak at 32 Da for O_2^+ molecular ions. The mass spectrum shows also peaks associated to Ga_nO_m molecular ions. Between 58 and 62 Da, a series of peaks indicates presence of Sn^{2+}, which was introduced as doping impurity during the growth.

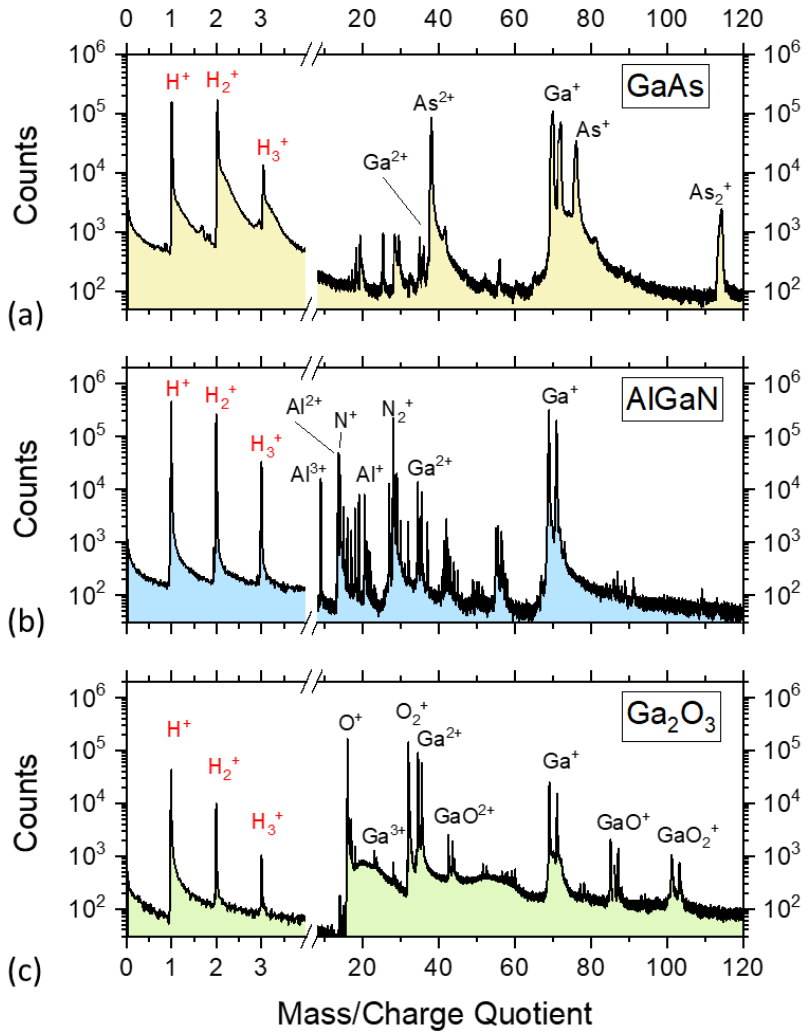

Figure 1. Typical mass spectra from APT analyses of (a) GaAs, (b) an AlGaN/GaN superlattice and (c) Ga_2O_3. The main spectral contributions, including the hydrogenic ions (in red) are indicated.

3. Results & Discussion

3.1. Relative abundances of H^+, H_2^+, H_3^+

The relative abundances of the H^+, H_2^+, H_3^+ ions have been studied as a function of the surface field in the three different materials systems.

3.1.1. Microscopic behavior in a III-nitride superlattice and role of the surface electric field.

The extensive analysis of nitride superlattices at constant detection ratio allows for the study of three different mechanisms of field variation. First, superlattices are composed of alternating layer of similar thickness (20 nm) but with a higher evaporation field in the $Al_yGa_{1-y}N$ than in the GaN layers [28,37]. When the apex surface meets the low-field GaN layers, the applied voltage decreases in order to keep the detection rate constant. Conversely, it increases when the surface intercepts an $Al_yGa_{1-y}N$ layer. Secondly, the field distribution also exhibits a strong dependence on the crystal orientation, as it has been demonstrated in different works [34,38]. In the present case, the crystal is grown with Ga-polarity and the [0001] axis almost coincides with the sample axis, and the field is highest in correspondence of this crystallographic pole. Thirdly, as mentioned, the field decreases on the average as the analysis proceeds because of the increase of the surface imaged on the detector.

The microscopic maps reported in Fig. 2-(a) are extracted from the reconstructed volume (see ref. [28] for details) of sample (Al,Ga)N-1 and refer to a 5 nm thick slice containing the axis of the sample. They show from left to right the maps of the Al site fraction, of the CSR(Ga), and of the relative abundances of H^+, H_2^+, H_3^+, respectively. The four detector space maps in Fig. 2-(b), on the other hand, are extracted from the fourth $Al_{0.7}Ga_{0.93}N$ layer from the bottom. In all these representations, a consistent picture emerges, which is quantitatively visualized in the correlation plot of Fig. 2-(c). The relative abundances of H^+, H_2^+, H_3^+ are unambiguously function of the surface electric field. This result is consistent with the early [17,39] and the latest research [11] on the

behavior of H species close to metallic surfaces under high electric field. The relative abundances of H^+ and H_2^+ are both close to 0.45 when the CSR(Ga) is as low as 0.01 (Field ~22 V/nm). For increasing field values, the amount of H_2^+ decreases, that of H^+ increases. Simultaneously, the relative abundance of H_3^+ decreases from 0.1 at low field to ~0.01 at higher field.

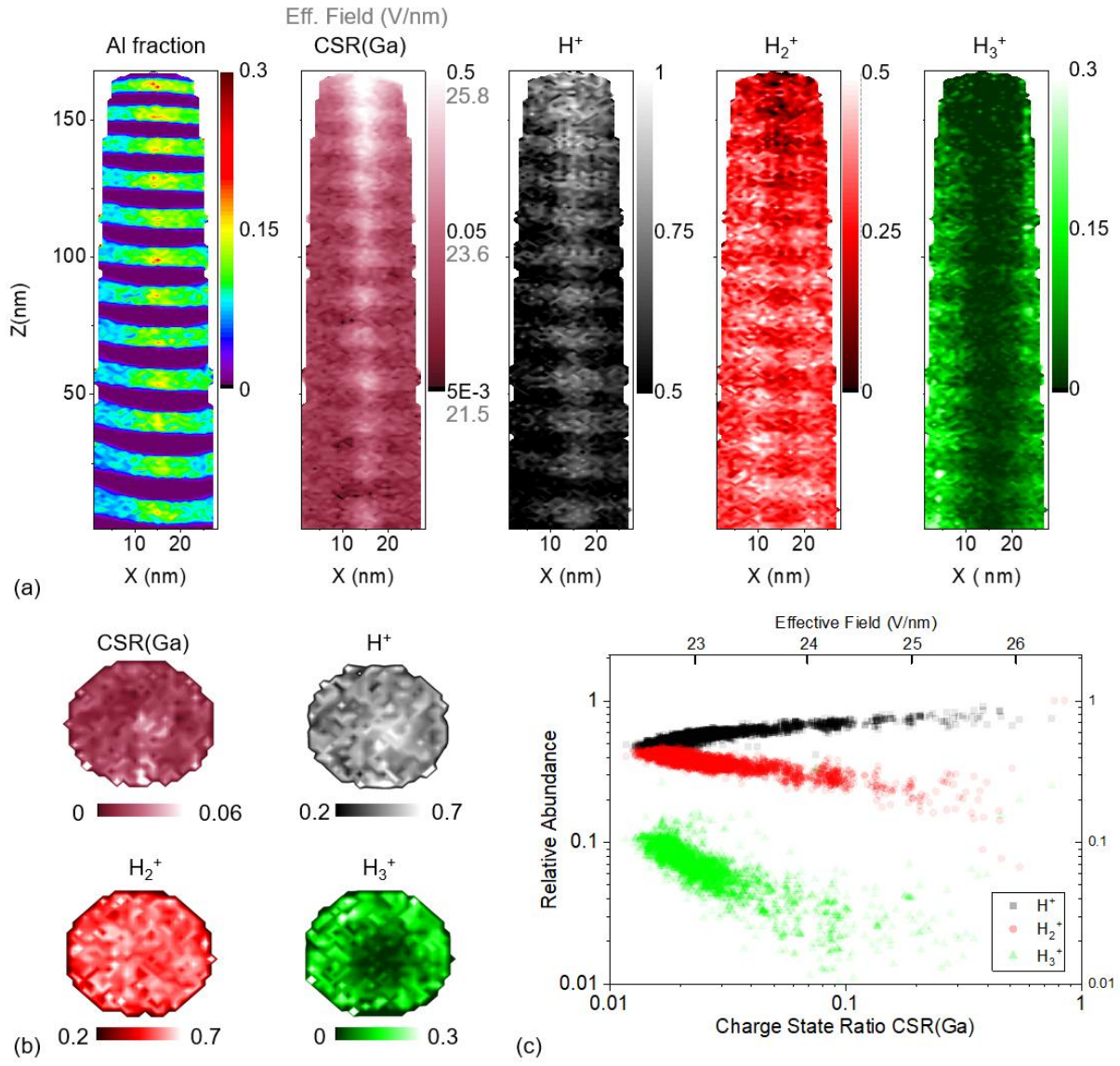

Figure 2 Microscopic behavior of hydrogen from the APT analysis of the (Al,Ga)N-1 superlattice. (a) Cross sectional maps extracted from the reconstructed volume of the analyzed specimen. From left to right: Al III-site fraction, Ga charge state ratio (in grey: effective surface field), relative abundances of H^+, H_2^+, H_3^+. (b) 2D map on the detector space extracted from the deepest $Al_{0.7}Ga_{0.93}N$ layer of Ga charge state ratio and relative abundances of H^+, H_2^+, H_3^+. (c) Correlation plot reporting the relative abundances of H^+, H_2^+, H_3^+ versus the Ga charge state ration and the effective surface field.

3.1.2. Trends in a large field interval over different compounds and metallization of apex surface.

The behavior of the abundances of H ions has been studied in other materials systems. The correlation of the abundances with the electric field for GaAs, (Al,Ga)N and Ga_2O_3 are shown in fig. 3. It is interesting to notice that the abundances follow common trends independently of the materials systems. This observation should not be considered as general (i.e., that the H abundances are functions of the electric field only), and are not influenced by surface chemistry. It has indeed been evidenced by Ai and Tsong that the relative abundances of H^+ and H_2^+ can be considered as closely independent of the crystallographic and chemical properties of the surface, while the abundance of H_3^+ exhibits a dependence on them [39]. These conclusions were drawn based on a study of 20 different metals. These early results also evidenced that the relative abundances of H^+ and H_2^+ cross at field levels of 25 V/nm, while in the present case the estimated surface field at which H^+ and H_2^+ are equally produced is slightly lower, around 22 V/nm. The abundances of H_3^+ were found to reach a maximum between 20 and 26 V/nm in metals (e.g. close to 21 V/nm in W and close to 25 V/nm in Ir and Ni) [39]. In this work, a diffused maximum of the H_3^+ abundance around 21-22 V/nm is obtained.

The main feature that can be underlined in this set of results is that the abundances are independent of the non-metallic element constituting the semiconductor. This observation is consistent with a recently formulated hypothesis, according to which laser-assisted field evaporation of GaN and InGaN takes place in a regime in which the surface is rich in metallic species [40]. This result is in agreement with the model describing the formation of laterally contracted metallic Ga bilayers that can be energetically favorable on GaN surfaces under Ga- rich conditions [41]. In the case of nitrides, the preferential loss of N by different evaporation channels could be the driving mechanism leading to Al- and Ga- rich conditions at the surface [27,33,36]. Intriguingly, metallic Ga bilayers are known to occur in very different situations, i.e. during the GaN growth by molecular beam epitaxy (MBE): in this case the Ga- rich conditions are assured by the regulation of the molecular fluxes impinging on the surface [42]. The formation of a Ga (Al, In) metallic layer on a III- N surface under high electric field also represents an alternative picture of the so- called "metallization" of apices of field- emission dielectric tips during APT analyses with respect to the proposed mechanism of hole accumulation induced by band bending and impact ionization[16]. The fact that the abundances of the H ions follow the same trends independently of the non-metallic elements may point out to similar surface metallization mechanisms in GaAs and Ga_2O_3 too. The present data are consistent with this hypothesis, which should be verified by independent measurements or supported by ab-initio calculations.

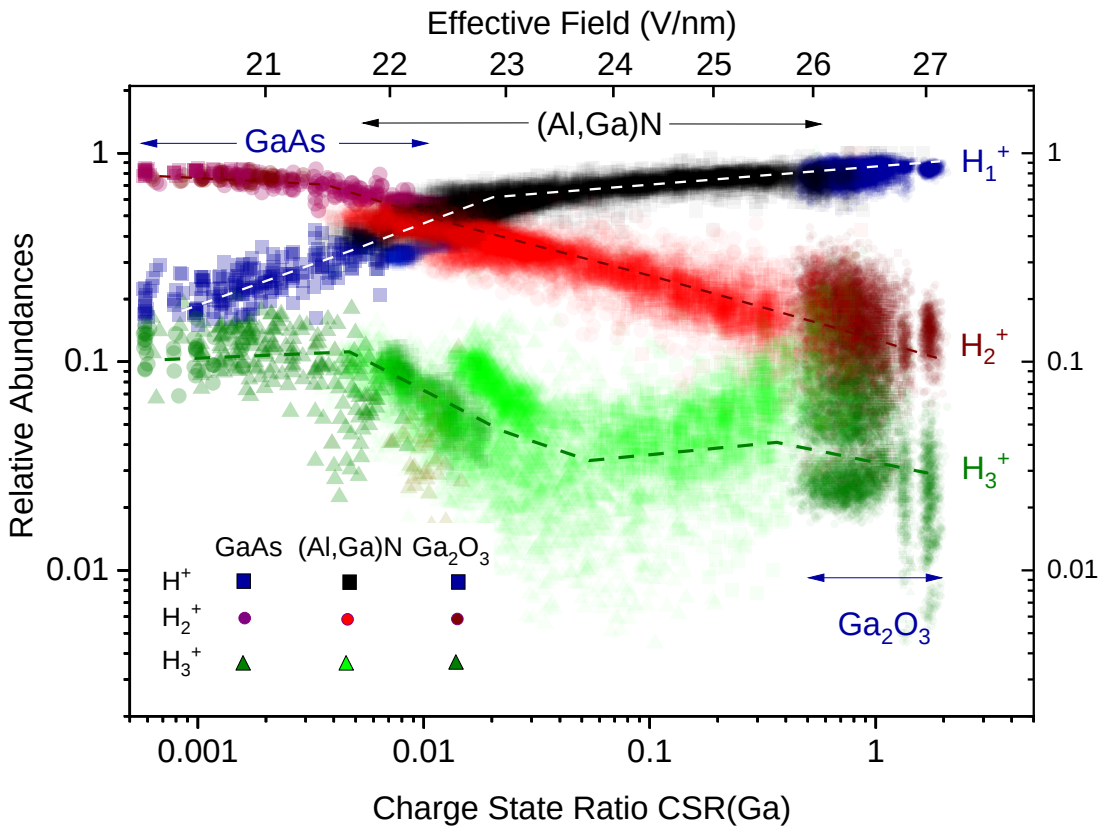

Figure 3. Fractions of hydrogenic ions H^+, H_2^+, H_3^+ over total detected hydrogenic ions for different materials systems reported versus the Ga charge state fraction and the surface effective field. The dashed lines are guides for the eye.

3.2. Cumulative abundance of hydrogen

Investigating the cumulative abundance of hydrogen as a function of the surface electric field represents a complementary approach with respect to the analysis of relative abundances.

3.2.1. Trends as a function of average surface field

The cumulative abundance of hydrogen ions has been analyzed in different materials systems. This quantity is determined by a set of parameters including the electric field, the residual partial pressure of H_2 in the analysis chamber, possibly also by the sample morphology and by its surface properties. This appears quite clearly in fig. 4, in which the cumulative abundance $\Phi(H)$ is reported as a function of the charge state ration CSR(Ga) and of the correspondingly estimated surface electric field. Unlike the relative abundances, which sketch the same trend across different materials systems, the trends of the cumulative abundances of H are different depending on the system. Nevertheless, the data of fig. 4 also show that within a single analysis and even within a single materials systems (i.e. (Al,Ga)N) there is a clear dependence of $\Phi(H)$ on the electric field: the flux of hydrogen is lower at the beginning of the analysis, for high electric field, and tends to increase when the field becomes lower. This behavior can be explained in quite simple terms. At lower field, indeed, H ionization occurs more frequently in correspondence with the laser pulse, and the ionized H can be correctly identified as contributing to the mass/charge peaks at 1, 2 and 3 Da in the mass/charge histogram (fig. 1). At higher field, this on-pulse ionization is progressively replaced by a continuous ionization or evaporation, producing ions that cannot be correctly identified and contribute to the increase of the background noise in the mass spectrum (in other terms, this is equivalent to being at higher field than the best-image field of field ion microscopy [43]). While the behavior of homogeneous samples, i.e. GaAs and Ga_2O_3, defines a clear trend with little dispersion along the field coordinate, this is not the case for the (Al,Ga)N superlattice samples. In the case of (Al,Ga)N superlattices, there is a larger dispersion of the data along the field coordinate. Even if not statistically relevant, a clearly off-trend cluster of data is present in the case of sample (Al, Ga)N-1. These data may conceal a more complex dependence of the cumulative abundance of hydrogen on the environmental parameters, and should be investigated by a microscopic imaging approach.

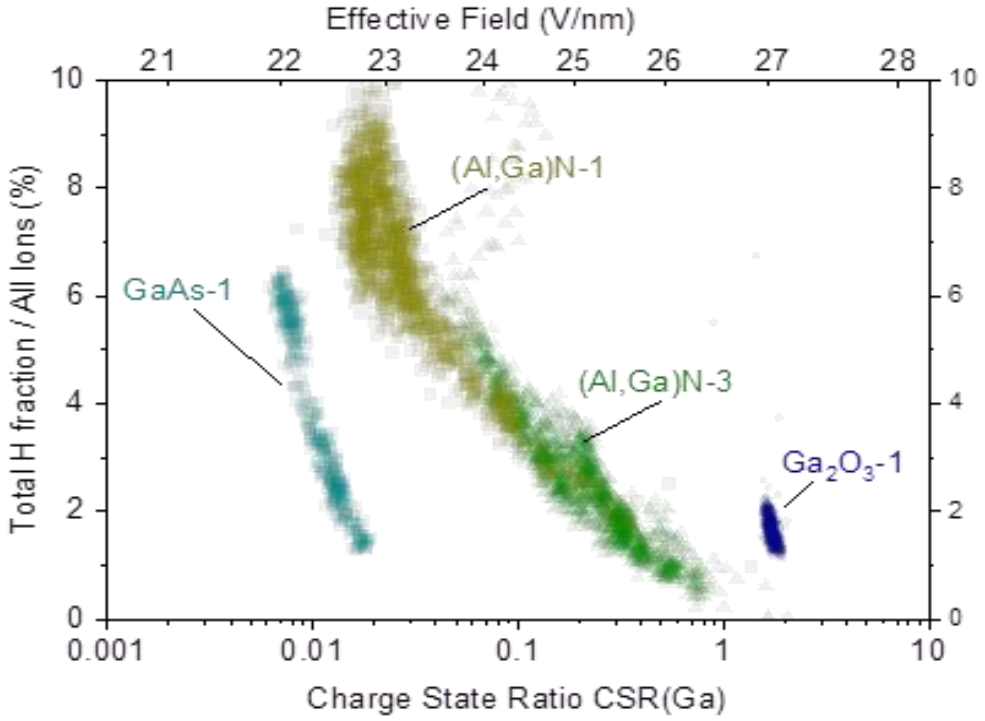

Figure 4. Total fraction of hydrogenic ions ($H^+ + H_2^+ + H_3^+$) over the total number of detected ions for different materials systems plotted versus the Ga charge state fraction and the effective surface field.

3.2.2. Microscopic behavior in a III-nitride superlattice

The data shown in fig. 5 illustrate the microscopic behavior of the cumulative abundance of hydrogen in an (Al,Ga)N superlattice. The Al fraction in the different layers and the CSR(Ga) maps in fig. 5-(a,b) respectively can be directly compared to the map of the cumulative H abundance reported in fig. 5-(c). In a similar way, it is possible to compare the detector space maps of the CSR(Ga) (fig. 5-(d)) and of Φ(H) in the map extracted from one of the AlGaN layers (indicated by the red arrow in fig. 5-(b)). If one considers the behavior of Φ(H) along the tip axis, it appears that, on the average, there is an anticorrelation between Φ(H) and the CSR(Ga), which

is the trend observed in the previous subsection and in fig. 4. However, the detector maps extracted from one of the AlGaN layers clearly indicates that in this representation Φ(H) increases when the CSR(Ga) also increases. Furthermore, it can also be seen that Φ(H) also decreases when the tip surface crosses an interface between an AlGaN layer (at higher field) and a GaN layer (at lower field).

This indicates that the cumulative abundance of H cannot be considered as a function of the surface electric field only, as would be the case of the relative abundances of the three H ionic species. Local variations of electric field also play an important role. Such a situation indicates that the total flux of hydrogen is also regulated by the supply of gas to the tip, which is, in turn, the outcome of gas pressure, field distribution, and diffusivity of adsorbed molecules – a problem that the current set of data allow pointing out but not yet solving.

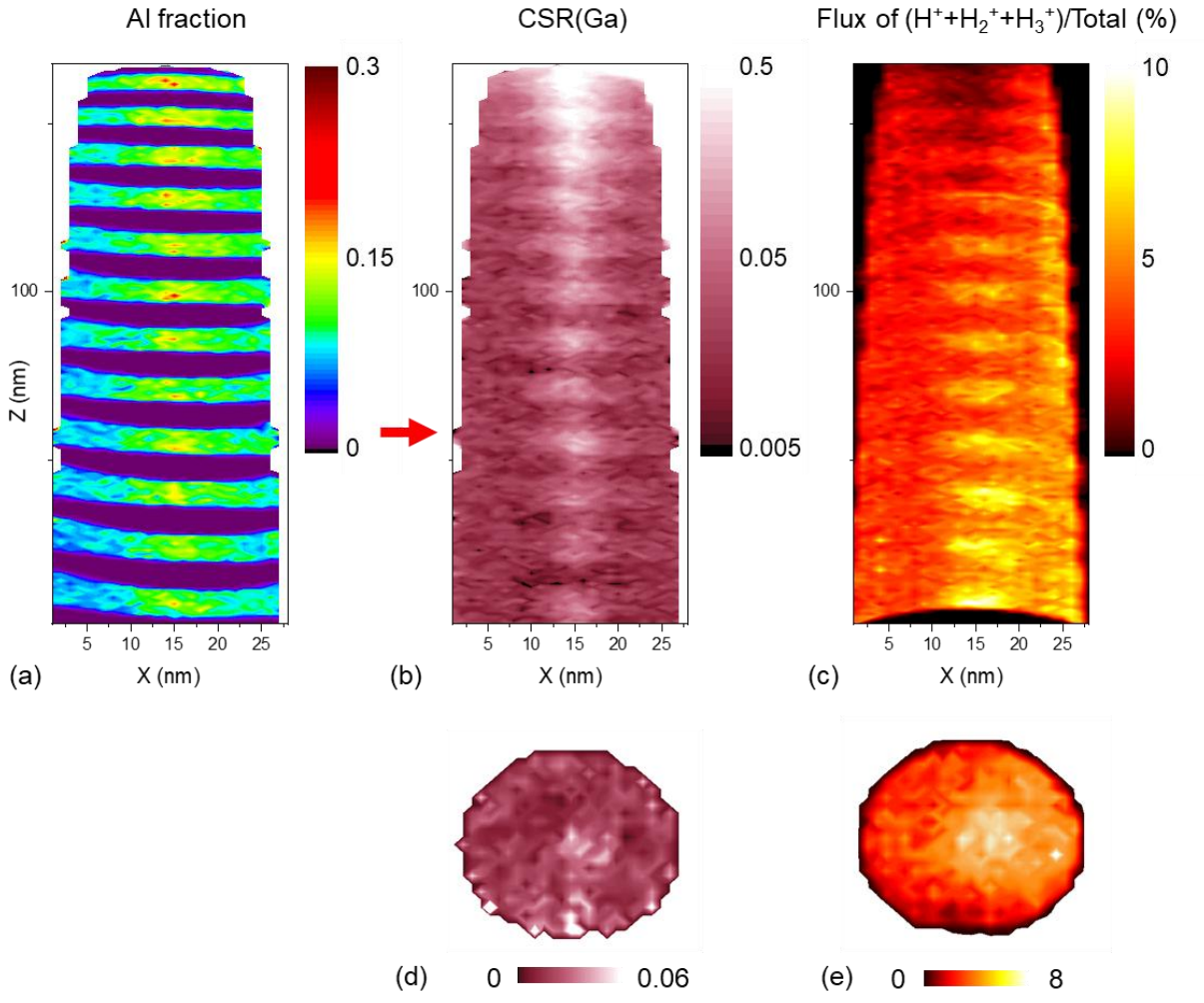

Figure 5. Microscopic behavior of the total flux of hydrogen molecules during the analysis of an AlGaN/GaN superlattice. (a-c) Cross sectional maps extracted from the reconstructed volume of the analyzed specimen of (a) Al fraction, (b) Ga charge state ratio, (c) Total fraction of hydrogenic ions ($H^+ + H_2^+ + H_3^+$) over the total number of detected ions. (d,e) Detector space histograms extracted from the AlGaN layer indicated by the red arrow in (b): (d) Ga charge state ration and (e) Total fraction of hydrogenic ions ($H^+ + H_2^+ + H_3^+$) over the total number of detected ions.

3.3. Hydrogen surface chemistry

A subset of chemical reactions involving H may yield two ionized or rapidly ionizable products, which could be detected following the same laser pulse. The statistical analysis of multiple detection events should therefore highlight the presence of such products, and possibly give further information on the reaction. In the following we will display and discuss the results obtained during APT of GaAs. The analysis of (Al,Ga)N samples at low field yields quantitatively similar results.

3.3.1. Analysis of multiple detection events in GaAs and in a III-nitride superlattice

A detail of the mass spectrum acquired during the analysis of the GaAs-1 sample, showing the mass/charge interval from 0 to 4 Da is reported in fig. 6-(a). The spectrum containing single detection events can be here compared to the spectrum containing multiple events. For this sample, the fraction of single detection events (including the ions from the matrix) was of 75 %. Concerning the mass peaks of hydrogenic species, the fraction of multiple events was 20 % for H^+, 5 % for H_2^+, and 9.5 % for H_3^+. These data should be considered with care, as they depend on the correlation of the hydrogenic species with all the detected species. The abundance of multiple events is not the same for the three species. In particular, the abundance of multiple events involving H_2^+ is significantly lower than that of the other two species.

In order to study the abundance of correlated H molecular ions, we focus on the correlation table 2 and on the correlation histogram of detection events reported in fig. 6-(b). The entries of table 2 are the correlation coefficients d_{ij} and the amounts of detected pairs p_{ij} in the intervals reported for each species, as defined in ref. [10] and adapted in ref.[33]. This method consists in comparing the number p_{ij} of each ion-pairs ij with the expected number of coincidences e_{ij} calculated under the

hypothesis of independent co-evaporation, so that $e_{ij} = e_i \times e_j$, where e_i is the fraction of the i-th species in the multiple-event mass spectrum. Both p_{ij} and e_{ij} are n × n matrices. The degree of correlation between measured and expected number of ion-pairs is provided by the following matrix:

$$d_{ij} = \frac{p_{ij} - e_{ij}}{e_{ij}}, \qquad (5)$$

where d_{ij} represents the degree of correlation (when $d_{ij} > 0$) or anti-correlation (when. $d_{ij} < 0$) between ion-pairs. Due to pile-up effects, the degree of self-correlation of all species is generally under-estimated, and, as a consequence, the degree of correlation of all other pairs is over-estimated. In order to correct for this effect, the diagonal values c_{ii} are artificially set equal to zero. Moreover, similarly to what is made in qui-squared tests, low p_{ij} entries (< 100) are considered as not statistically significant. Notice that the sampling interval for the H^+ ions on the m_1 axis is set as significantly smaller than 1 (the default choice for the other intervals) in order to eliminate possible contributions from the pairs populating the diagonal, as these may stem from a variety of other processes[10]. The most relevant result is a strong correlation of H^+-H_3^+ pairs.

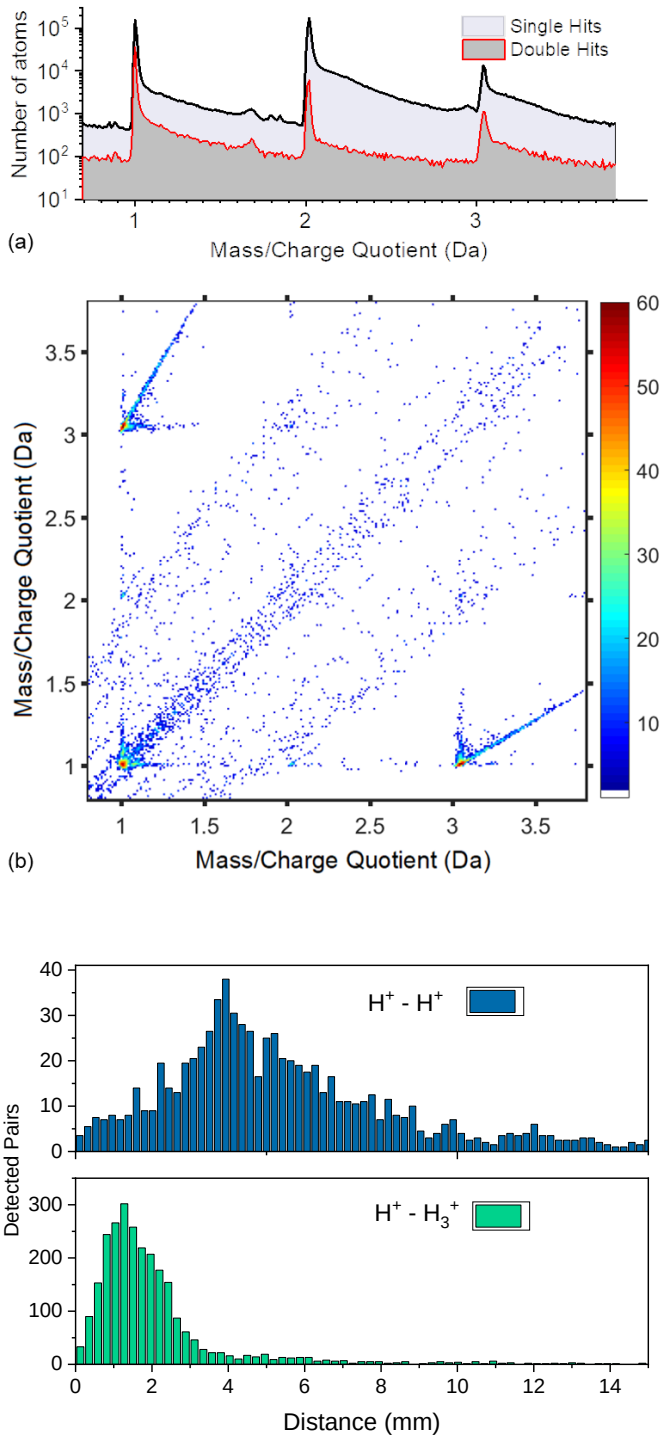

Fig. 6. (a) Detail of the mass spectra from the analysis of GaAs distinguishing the single and double events in the region containing the H^+, H_2^+, H_3^+ species. (b) Multiple-event correlation histogram for the region enclosing the H^+, H_2^+, H_3^+ species. (c) Distance distributions of multiple events corresponding to the detection of H^+-H^+ pairs (top) and H^+-H_3^+ pairs (bottom).

Table 2. Correlation table of ion pairs involving atomic and molecular hydrogen

	Correlation coefficient d_{ij} (number of pairs per $m_1.m_2$ interval p_{ij})			Number of pairs per interval on the m_1 axis (n_i)
$[m_2]$ / $[m_1]$	**H^+ [0.95, 1.95]**	**H_2^+ [1.95, 2.95]**	**H_3^+ [2.95, 3.95]**	
H^+ [0.95, 1.15]	0 (900)	7.7 (351)	28 (2372)	3623
H_2^+[1.95, 2.95]	7.7 (351)	0 (41)	-10 (24)	416
H_3^+[2.95, 3.95]	28 (2372)	-10 (24)	0 (25)	2421

These features may be further analyzed within the correlation histogram of fig. 6-(b), of which table 2 is a synthesis. In this plot we notice that different qualitative behaviors characterize the different ion pairs. Focusing on the intervals with the largest number of pairs, we notice that the behavior of the H^+-H^+ and of the H^+-H_3^+ pairs is quite similar, with a main peak centered on (m_H, m_H) and (m_H, m_{H3}), respectively, followed by a diagonal track corresponding to the thermal tail of simultaneous delayed evaporations, and with two minor horizontal and vertical track corresponding to the delayed evaporation of a second ion after the first evaporated on-pulse. A further insight into the behavior of the ion pair is yielded by the comparison of the histograms of the distances on the detector of each pair, as reported in fig. 6-(c), top and bottom panels. The histogram for H^+-H^+ indicates an average distance of around 4 mm, while this value drops to 1.8 mm for H^+-H_3^+, a behavior that could be explained in terms of a larger impact of Coulomb repulsion for the fragments of a dissociation reaction having equal masses (H^+-H^+) than for fragments with different masses (H^+-H_3^+). Figure 7 reports the position of both components of each detected pair within a 2 cm diameter circle centered at the detector center for the two cases

of (a) H^+-H^+ and (b) H^+-H_3^+ pairs. These diagrams visually confirm the distance distributions resumed in the histograms of fig. 6-(c), and qualitatively indicate the randomness of the orientation of the pair in the detector space.

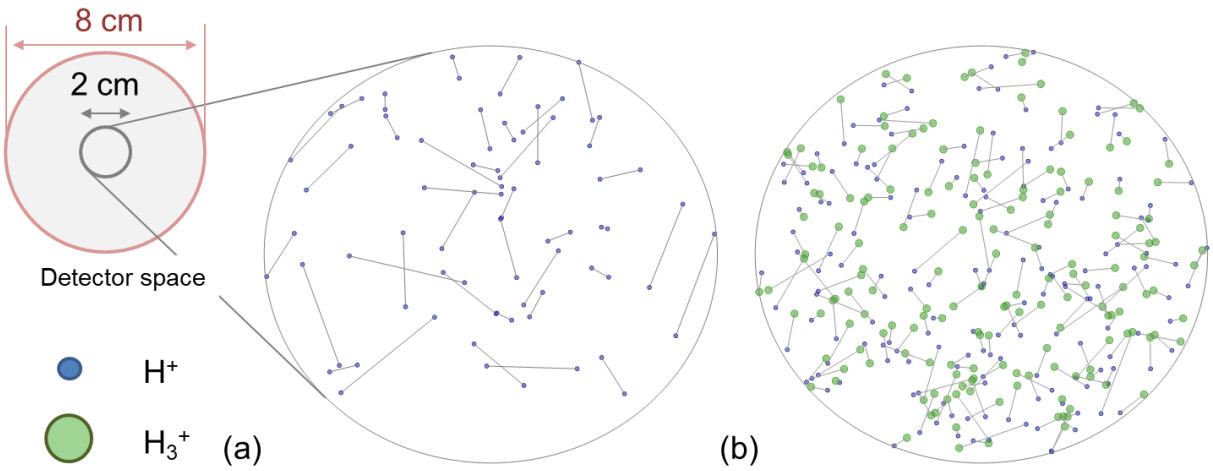

Fig. 7 Representation of a subset of detected ion pairs within a 2 cm diameter circle centered in the center of the detector. (a) Detected H^+-H^+ pairs and (b) detected H^+-H_3^+ pairs.

3.3.2. Discussion about reactions involving H_2.

The analysis of correlated detection of ion pairs can be interpreted in the context of proposed or novel mechanisms for the formation of these molecules on the evaporating field-emission tip sample. H_2^+ is mainly produced during simple ionization events of the adsorbed H_2 molecules, without any molecular dissociation, without reactions with the surface, and without the direct assistance of field evaporation of the matrix constituents. On the other hand, H^+ and H_3^+ are produced upon chemical reactions.

The mechanism originally proposed by Ernst and Block, who studied temperature- or electron-stimulated field desorption under steady state conditions within a magnetic-sector-field mass spectrometer, is the following [18,44]:

$H_2(\text{f-ad}) + H(\text{c-s}) \rightarrow H_3^+(g) + e^-(Me)$,

where « g » indicates that the species is in a gaseous phase, « f-ad » that the species is (weakly) field adsorbed, « c-s » that the species is chemisorbed, while « Me » indicates that the electrons set free are collected into the metal phase (we refer to a metal phase even if we are dealing with dielectrics as we are in strong field conditions, and this modifies the properties of the surfaces). This reaction is suggested based on the spectroscopic analysis of ion appearance energies and results in the emission of the molecular ion H_3^+ only.

Tsong and Kinkus studied the phenomenon of H_3^+ production in conditions more similar to ours, i.e. in a pulsed-laser atom probe. They propose an alternative mechanism, i.e. the thermally activated ionization of adsorbed H_3 molecules which have previously formed at the emitter surface[45].

Both mechanisms may be valid, in the respective set of experimental conditions. The main difference between our work and the previous ones resides mainly in our possibility to analyze multiple ion events, with an access to the possible correlations between different ions. In our case, a subset of the produced H_3^+ ions is at least detected together with H^+ ions following the same laser pulse, and that moreover these events are extremely close in the detector space, which means that the ions stem from a very localized region, i.e. within a radius of around 2 nm. This is the range that we can estimate through the ratio between the detector diameter and the diameter of the imaged portion of the analyzed GaAs tip; however, this could only be an upper bound if we

consider that coulomb repulsion may occur between charged particles if both detected ions are produced simultaneously. This strongly suggests a reaction producing H_3^+ and H^+ upon the same laser pulse. We can therefore propose a further reaction mechanism, i.e.

$$2H_2(\text{f-ad}) \rightarrow H^+(g) + H_3^+(g) + 2e^-(\text{Me}) \qquad (6)$$

It should be underlined that this mechanism could be decomposed into several sequential steps, for instance the production of one ionized and one neutral species followed by the ionization of the other species:

$$2H_2(\text{f-ad}) \rightarrow H(\text{f-ad}) + H_3^+(g) + e^-(\text{Me}) \rightarrow H^+(g) + H_3^+(g) + 2e^-(\text{Me}) \qquad (7)$$

or

$$2H_2(\text{f-ad}) \rightarrow H^+(g) + H_3(\text{f-ad}) + e^-(\text{Me}) \rightarrow H^+(g) + H_3^+(g) + 2e^-(\text{Me}). \qquad (8)$$

The current data do not indicate whether the production of the H_3^+ and of the H^+ occurs simultaneously or as a sequential process. The correlation histogram of fig. 6-(b) indicates that the production events are simultaneous within the uncertainty of the time-of-flight spectroscopy of these species, which is of the order of 100 ns. This does not exclude a sequential reaction taking place within a smaller time scale. The impact diagram of fig. 7-(b) allows imaging not only the products of individual reactions, but also estimating the location of the original reagent on the field emitter surface with a precision depending on the actual tip radius, but which is expected to be of the order of one to several nanometers. It is worth noticing that this capability of imaging chemical surface reactions could be more extensively applied in future APT-based analyses of gas-surface interactions.

4. Conclusions and outlook

We studied the microscopic behavior of parasitic hydrogen the surface of homogeneous or heterostructured compound semiconductor field emitter samples, all containing the Ga species, analyzed by laser-assisted APT. The relative abundances of the ionic species H^+, H_2^+, H_3^+ exhibit a clear dependence on the microscopic electric field. In the case of Ga-containing semiconductors, the relative abundances of H^+ and H_2^+ follow a common trend, independently of the non-metallic component of the matrix., with H_2^+ being the majority species at low field, while H^+ becomes the majority species at high field. Molecular H_3^+ is generally found at low/intermediate field intensities (between 20 and 22 V/nm) in relative fractions up to 10 %. On the other hand, the dependence of the total H flux on the electric field exhibits a more complex behavior which depends also on the spatial direction of the variation of the field (in-depth or on-surface).

The analysis of multiple detection events provides further insight into surface chemistry. Noticeably, H^+-H_3^+ ion pairs are both correlated in number and separated by very small distances on the detector space, suggesting a possible reaction $2H_2 \rightarrow H_3^+ + H^+ + 2e^-$ taking place on the field emitter surface. Individual reactions may be directly visualized on the detector space and thus, through a projection law, on the actual emitter surface.

In perspective, multiple hit analysis may also offer some insight into the interaction of H with the components of the matrix. This may be of particular interest in those cases in which the presence of H does not directly translate in the presence of hydrides (AlH_n^+ hydride molecular ions form, for instance, in Al). The methods applied here may be developed for the study of materials for hydrogen storage or for heterogeneous field-assisted catalysis.

Author Contributions

The manuscript was written through contributions of all authors. All authors have given approval to the final version of the manuscript.

Acknowledgements

This work was funded by the French National Research Agency (ANR) in the framework of the projects EMC3 Labex BREAKING-AP and by European Union with European Regional Development Fund (ERDF) and by Region Normandie in the framework of the project RIN IFROST.

REFERENCES

(1) Turner, J. A. Sustainable Hydrogen Production. *Science* **2004**, *305* (5686), 972–974. https://doi.org/10.1126/science.1103197.

(2) Daw, M. S.; Baskes, M. I. Semiempirical, Quantum Mechanical Calculation of Hydrogen Embrittlement in Metals. *Phys. Rev. Lett.* **1983**, *50* (17), 1285–1288. https://doi.org/10.1103/PhysRevLett.50.1285.

(3) Takahashi, J.; Kawakami, K.; Tarui, T. Direct Observation of Hydrogen-Trapping Sites in Vanadium Carbide Precipitation Steel by Atom Probe Tomography. *Scr. Mater.* **2012**, *67* (2), 213–216. https://doi.org/10.1016/j.scriptamat.2012.04.022.

(4) Chen, Y.-S.; Haley, D.; Gerstl, S. S. A.; London, A. J.; Sweeney, F.; Wepf, R. A.; Rainforth, W. M.; Bagot, P. a. J.; Moody, M. P. Direct Observation of Individual Hydrogen Atoms at Trapping Sites in a Ferritic Steel. *Science* **2017**, *355* (6330), 1196–1199. https://doi.org/10.1126/science.aal2418.

(5) Stavola, M.; Bergman, K.; Pearton, S. J.; Lopata, J. Hydrogen Motion in Defect Complexes: Reorientation Kinetics of the B-H Complex in Silicon. *Phys. Rev. Lett.* **1988**, *61* (24), 2786–2789. https://doi.org/10.1103/PhysRevLett.61.2786.

(6) Van de Walle, C. G.; Neugebauer, J. Hydrogen in Semiconductors. *Annu. Rev. Mater. Res.* **2006**, *36* (1), 179–198. https://doi.org/10.1146/annurev.matsci.36.010705.155428.

(7) Felfer, P. J. A Toolchain for the Analysis of Hydrogen in Materials at the Atomic Scale. *Microsc. Microanal.* **2019**, *25* (S2), 278–279. https://doi.org/10.1017/S1431927619002125.

(8) Chang, Y. H.; Mouton, I.; Stephenson, L.; Ashton, M.; Zhang, G. K.; Szczpaniak, A.; Lu, W. J.; Ponge, D.; Raabe, D.; Gault, B. Quantification of Solute Deuterium in Titanium Deuteride by Atom Probe Tomography with Both Laser Pulsing and High-Voltage Pulsing: Influence of the Surface Electric Field. *New J. Phys.* **2019**, *21* (5), 053025. https://doi.org/10.1088/1367-2630/ab1c3b.

(9) Tsong, T. T. Atom-Probe Field Ion Microscopy. *At.-Probe Field Ion Microsc. Tien T Tsong Pp 397 ISBN 0521363799 Camb. UK Camb. Univ. Press August 1990* **1990**.

(10) Saxey, D. W. Correlated Ion Analysis and the Interpretation of Atom Probe Mass Spectra. *Ultramicroscopy* **2011**, *111* (6), 473–479. https://doi.org/10.1016/j.ultramic.2010.11.021.

(11) Sundell, G.; Thuvander, M.; Andrén, H.-O. Hydrogen Analysis in APT: Methods to Control Adsorption and Dissociation of H2. *Ultramicroscopy* **2013**, *132*, 285–289. https://doi.org/10.1016/j.ultramic.2013.01.007.

(12) Suzor-Weiner, A.; Schneider, I. F. Mystery of an Interstellar Ion. *Nature* **2001**, *412* (6850), 871–872. https://doi.org/10.1038/35091186.

(13) Oka, T. Interstellar H3+. *Proc. Natl. Acad. Sci.* **2006**, *103* (33), 12235–12242. https://doi.org/10.1073/pnas.0601242103.

(14) Schwarz, T. M.; Weikum, E. M.; Meng, K.; Hadjixenophontos, E.; Dietrich, C. A.; Kästner, J.; Stender, P.; Schmitz, G. Field Evaporation and Atom Probe Tomography of Pure Water Tips. *Sci. Rep.* **2020**, *10* (1), 20271. https://doi.org/10.1038/s41598-020-77130-x.

(15) El-Zoka, A. A.; Kim, S.-H.; Deville, S.; Newman, R. C.; Stephenson, L. T.; Gault, B. Enabling Near-Atomic–Scale Analysis of Frozen Water. *Sci. Adv.* **2020**, *6* (49), eabd6324. https://doi.org/10.1126/sciadv.abd6324.

(16) Silaeva, E. P.; Arnoldi, L.; Karahka, M. L.; Deconihout, B.; Menand, A.; Kreuzer, H. J.; Vella, A. Do Dielectric Nanostructures Turn Metallic in High-Electric Dc Fields? *Nano Lett.* **2014**, *14* (11), 6066–6072. https://doi.org/10.1021/nl502715s.
(17) Tsong, T. T.; Kinkus, T. J.; Ai, C. F. Field Induced and Surface Catalyzed Formation of Novel Ions : A Pulsed- laser Time- of- flight Atom- probe Study. *J. Chem. Phys.* **1983**, *78* (7), 4763–4775. https://doi.org/10.1063/1.445276.
(18) Ernst, N.; Block, J. H. Temperature Programmed Field Desorption of Protonated Hydrogen from Rhodium and Tungsten. *Surf. Sci.* **1983**, *126* (1), 397–404. https://doi.org/10.1016/0039-6028(83)90734-3.
(19) Haley, D.; McCarroll, I.; Bagot, P. A. J.; Cairney, J. M.; Moody, M. P. A Gas-Phase Reaction Cell for Modern Atom Probe Systems. *Microsc. Microanal.* **2019**, *25* (2), 410–417. https://doi.org/10.1017/S1431927618016240.
(20) Lambeets, S. V.; Visart de Bocarmé, T.; Perea, D. E.; Kruse, N. Directional Gateway to Metal Oxidation: 3D Chemical Mapping Unfolds Oxygen Diffusional Pathways in Rhodium Nanoparticles. *J. Phys. Chem. Lett.* **2020**, *11* (8), 3144–3151. https://doi.org/10.1021/acs.jpclett.0c00321.
(21) McCarroll, I. E.; Haley, D.; Thomas, S.; Meier, M. S.; Bagot, P. A. J.; Moody, M. P.; Birbilis, N.; Cairney, J. M. The Effect of Hydrogen on the Early Stages of Oxidation of a Magnesium Alloy. *Corros. Sci.* **2020**, *165*, 108391. https://doi.org/10.1016/j.corsci.2019.108391.
(22) Di Russo, E.; Dalapati, P.; Houard, J.; Venturi, L.; Blum, I.; Moldovan, S.; Le Biavan, N.; Lefebvre, D.; Hugues, M.; Chauveau, et al., L. Super-Resolution Optical Spectroscopy of Nanoscale Emitters within a Photonic Atom Probe. *Nano Lett.* **2020**, *20* (12), 8733–8738. https://doi.org/10.1021/acs.nanolett.0c03584.
(23) Houard, J.; Normand, A.; Di Russo, E.; Bacchi, C.; Dalapati, P.; Beainy, G.; Moldovan, S.; Da Costa, G.; Delaroche, F.; Vaudolon, et al. L. A Photonic Atom Probe Coupling 3D Atomic Scale Analysis with in Situ Photoluminescence Spectroscopy. *Rev. Sci. Instrum.* **2020**, *91* (8), 083704. https://doi.org/10.1063/5.0012359.
(24) Cocke, D. L.; Chuah, G. K.; Kruse, N.; Block, J. H. Copper Oxidation and Surface Copper Oxide Stability Investigated by Pulsed Field Desorption Mass Spectrometry. *Appl. Surf. Sci.* **1995**, *84* (2), 153–161. https://doi.org/10.1016/0169-4332(94)00467-6.
(25) Lambeets, S. V.; Kautz, E. J.; Wirth, M. G.; Orren, G. J.; Devaraj, A.; Perea, D. E. Nanoscale Perspectives of Metal Degradation via In Situ Atom Probe Tomography. *Top. Catal.* **2020**, *63* (15), 1606–1622. https://doi.org/10.1007/s11244-020-01367-z.
(26) Kingham, D. R. The Post-Ionization of Field Evaporated Ions: A Theoretical Explanation of Multiple Charge States. *Surf. Sci.* **1982**, *116* (2), 273–301. https://doi.org/10.1016/0039-6028(82)90434-4.
(27) Mancini, L.; Amirifar, N.; Shinde, D.; Blum, I.; Gilbert, M.; Vella, A.; Vurpillot, F.; Lefebvre, W.; Lardé, R.; Talbot, et al. Composition of Wide Bandgap Semiconductor Materials and Nanostructures Measured by Atom Probe Tomography and Its Dependence on the Surface Electric Field. *J. Phys. Chem. C* **2014**, *118* (41), 24136–24151. https://doi.org/10.1021/jp5071264.
(28) Di Russo, E.; Moyon, F.; Gogneau, N.; Largeau, L.; Giraud, E.; Carlin, J.-F.; Grandjean, N.; Chauveau, J. M.; Hugues, M.; Blum, et al. Composition Metrology of Ternary Semiconductor Alloys Analyzed by Atom Probe Tomography. *J. Phys. Chem. C* **2018**, *122* (29), 16704–16714. https://doi.org/10.1021/acs.jpcc.8b03223.

(29) Kracht, M.; Karg, A.; Schörmann, J.; Weinhold, M.; Zink, D.; Michel, F.; Rohnke, M.; Schowalter, M.; Gerken, B.; Rosenauer, et al. Tin-Assisted Synthesis of Ga_2O_3 by Molecular Beam Epitaxy. *Phys. Rev. Appl.* **2017**, *8* (5), 054002. https://doi.org/10.1103/PhysRevApplied.8.054002.
(30) Blum, I.; Cuvilly, F.; Lefebvre-Ulrikson, W. Chapter Four - Atom Probe Sample Preparation. In *Atom Probe Tomography*; Academic Press, 2016; pp 97–121. https://doi.org/10.1016/B978-0-12-804647-0.00004-8.
(31) Da Costa, G.; Vurpillot, F.; Bostel, A.; Bouet, M.; Deconihout, B. Design of a Delay-Line Position-Sensitive Detector with Improved Performance. *Rev. Sci. Instrum.* **2005**, *76*, 013304–013304. https://doi.org/10.1063/1.1829975.
(32) Costa, G. D.; Wang, H.; Duguay, S.; Bostel, A.; Blavette, D.; Deconihout, B. Advance in Multi-Hit Detection and Quantization in Atom Probe Tomography. *Rev. Sci. Instrum.* **2012**, *83*, 123709–123709. https://doi.org/10.1063/1.4770120.
(33) Russo, E. D.; Blum, I.; Houard, J.; Costa, G. D.; Blavette, D.; Rigutti, L. Field-Dependent Measurement of GaAs Composition by Atom Probe Tomography. *Microsc. Microanal.* **2017**, 1–9. https://doi.org/10.1017/S1431927617012582.
(34) Riley, J. R.; Bernal, R. A.; Li, Q.; Espinosa, H. D.; Wang, G. T.; Lauhon, L. J. Atom Probe Tomography of A-Axis GaN Nanowires: Analysis of Nonstoichiometric Evaporation Behavior. *ACS Nano* **2012**, *6* (5), 3898–3906. https://doi.org/10.1021/nn2050517.
(35) Riley, J. R.; Detchprohm, T.; Wetzel, C.; Lauhon, L. J. On the Reliable Analysis of Indium Mole Fraction within InxGa1−xN Quantum Wells Using Atom Probe Tomography. *Appl. Phys. Lett.* **2014**, *104* (15), 152102. https://doi.org/10.1063/1.4871510.
(36) Russo, E. D.; Blum, I.; Houard, J.; Gilbert, M.; Da Costa, G.; Blavette, D.; Rigutti, L. Compositional Accuracy of Atom Probe Tomography Measurements in GaN: Impact of Experimental Parameters and Multiple Evaporation Events. *Ultramicroscopy* **2018**, *187*, 126–134. https://doi.org/10.1016/j.ultramic.2018.02.001.
(37) Rigutti, L.; Mancini, L.; Hernández-Maldonado, D.; Lefebvre, W.; Giraud, E.; Butté, R.; Carlin, J. F.; Grandjean, N.; Blavette, D.; Vurpillot, F. Statistical Correction of Atom Probe Tomography Data of Semiconductor Alloys Combined with Optical Spectroscopy: The Case of Al0.25Ga0.75N. *J. Appl. Phys.* **2016**, *119* (10), 105704. https://doi.org/10.1063/1.4943612.
(38) Rigutti, L.; Blum, I.; Shinde, D.; Hernández-Maldonado, D.; Lefebvre, W.; Houard, J.; Vurpillot, F.; Vella, A.; Tchernycheva, M.; Durand, et al. Correlation of Microphotoluminescence Spectroscopy, Scanning Transmission Electron Microscopy, and Atom Probe Tomography on a Single Nano-Object Containing an InGaN/GaN Multiquantum Well System. *Nano Lett.* **2014**, *14* (1), 107–114. https://doi.org/10.1021/nl4034768.
(39) Chi-fong Ai; Tsong, T. T. Field Promoted and Surface Catalyzed Formation of H3 and NH3 on Transition Metal Surfaces: A Pulsed-Laser Imaging Atom-Probe Study. *Surf. Sci.* **1984**, *138* (2), 339–360. https://doi.org/10.1016/0039-6028(84)90252-8.
(40) Di Russo, E.; Cherkashin, N.; Korytov, M.; Nikolaev, A. E.; Sakharov, A. V.; Tsatsulnikov, A. F.; Bonef, B.; Blum, I.; Houard, J.; Da Costa, et al. Compositional Accuracy in Atom Probe Tomography Analyses Performed on III-N Light Emitting Diodes. *J. Appl. Phys.* **2019**, *126* (12), 124307. https://doi.org/10.1063/1.5113799.
(41) Northrup, J. E.; Neugebauer, J.; Feenstra, R. M.; Smith, A. R. Structure of GaN(0001): The Laterally Contracted Ga Bilayer Model. *Phys. Rev. B* **2000**, *61* (15), 9932–9935. https://doi.org/10.1103/PhysRevB.61.9932.

(42) Adelmann, C.; Brault, J.; Mula, G.; Daudin, B.; Lymperakis, L.; Neugebauer, J. Gallium Adsorption on (0001) GaN Surfaces. *Phys. Rev. B* **2003**, *67* (16), 165419. https://doi.org/10.1103/PhysRevB.67.165419.
(43) Danoix, F.; Vurpillot, F. Chapter Three - Basics of Field Ion Microscopy. In *Atom Probe Tomography*; Lefebvre-Ulrikson, W., Vurpillot, F., Sauvage, X., Eds.; Academic Press, 2016; pp 73–95. https://doi.org/10.1016/B978-0-12-804647-0.00003-6.
(44) Ernst, N.; Block, J. H. Electron-Stimulated Field Desorption of Diatomic and Triatomic Hydrogen. *Phys. Rev. B* **1984**, *29* (12), 7092–7095. https://doi.org/10.1103/PhysRevB.29.7092.
(45) Tsong, T. T.; Kinkus, T. J. Energy Distributions of Pulsed-Laser Field-Desorbed Gaseous Ions and Field-Evaporated Metal Ions: A Direct Time-of-Flight Measurement. *Phys. Rev. B* **1984**, *29* (2), 529–542. https://doi.org/10.1103/PhysRevB.29.529.

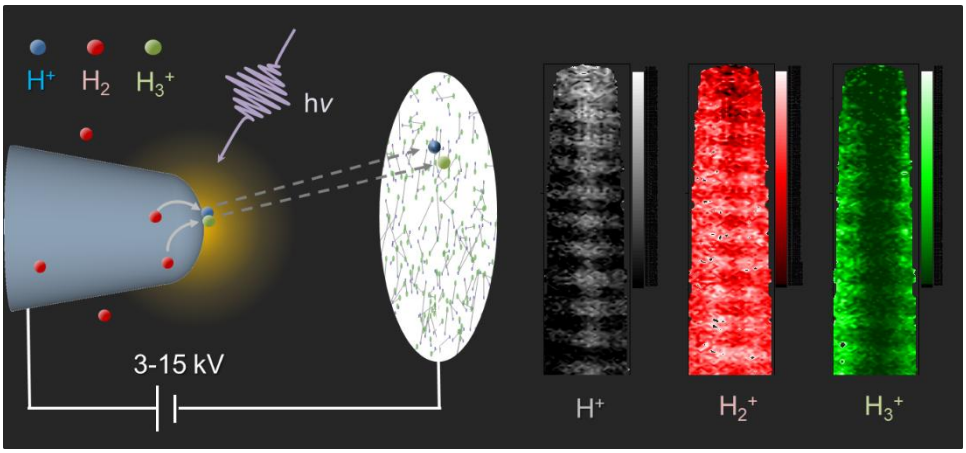

TOC Graphic